

## Experimental Evidence for Nonaxisymmetric Magnetorotational Instability in a Rotating Liquid Metal Exposed to an Azimuthal Magnetic Field

Martin Seilmayer, Vladimir Galindo, Gunter Gerbeth, Thomas Gundrum, and Frank Stefani\*  
*Helmholtz-Zentrum Dresden-Rossendorf, P.O. Box 510119, D-01314 Dresden, Germany*

Marcus Gellert, Günther Rüdiger, and Manfred Scholtz  
*Leibniz-Institut für Astrophysik Potsdam, An der Sternwarte 16, D-14482 Potsdam, Germany*

Rainer Hollerbach

*Department of Applied Mathematics, University of Leeds, Leeds LS2 9JT, United Kingdom*  
(Received 28 November 2013; revised manuscript received 5 May 2014; published 10 July 2014)

The azimuthal version of the magnetorotational instability (MRI) is a nonaxisymmetric instability of a hydrodynamically stable differentially rotating flow under the influence of a purely or predominantly azimuthal magnetic field. It may be of considerable importance for destabilizing accretion disks, and plays a central role in the concept of the MRI dynamo. We report the results of a liquid metal Taylor-Couette experiment that shows the occurrence of an azimuthal MRI in the expected range of Hartmann numbers.

DOI: [10.1103/PhysRevLett.113.024505](https://doi.org/10.1103/PhysRevLett.113.024505)

PACS numbers: 47.20.Qr, 52.30.-q, 97.10.Gz

The magnetorotational instability (MRI) is widely accepted as the main source of turbulence and angular momentum transport in accretion disks around protostars and black holes. Although discovered by Velikhov [1] as early as 1959, its relevance for the evolution of stellar systems, x-ray binaries, and active galactic nuclei was only recognized by Balbus and Hawley in 1991 [2]. While most of the early MRI studies had considered a uniform axial magnetic field threading the flow (nonzero net flux), recent focus [3] has shifted slightly to the case of azimuthal fields (zero net flux). One reason for this lies in the interesting concept of a subcritical MRI dynamo, in which the MRI-triggering field is partly sustained by the MRI-driven turbulence itself [4]. Another possible application is related to the high values of “artificial viscosity” that are needed to explain the slowing down of stellar cores after the collapse towards their red giant stage [5].

In magnetohydrodynamic stability problems of this kind, the magnetic Prandtl number,  $Pm$ , the ratio of the fluid’s kinematic viscosity to its magnetic diffusivity, can play a crucial role. For  $Pm \geq 1$  both nonzero and zero net flux versions of the MRI operate very effectively and robustly, whereas for  $Pm \ll 1$  both are far more delicate, involving not only numerical convergence issues, but also real physical effects such as the role of stratification or boundary conditions [6].

The discovery of the helical MRI (HMRI) by Hollerbach and Rüdiger in 2005 [7] spurred additional interest in the small  $Pm$  limit. For an appropriate combination of axial and azimuthal magnetic fields, the HMRI was shown to work even in the inductionless limit  $Pm \rightarrow 0$ , since it depends only on the Reynolds number,  $Re$ , and the Hartmann number,  $Ha$ . This is in contrast with the standard MRI

(SMRI) which requires both the magnetic Reynolds number  $Rm = Pm Re$  and the Lundquist number  $S = Pm^{1/2} Ha$  to be at least  $O(1)$ , and is correspondingly difficult to observe in the laboratory [8].

It is of interest also to consider the possibility of a (nonaxisymmetric) MRI operating in a purely azimuthal field [9], a configuration that has come to be known as the azimuthal MRI (AMRI) [10]. It was initially believed that the AMRI operates only in the same  $(Rm, S) > O(1)$  parameter regime as the SMRI, and would be experimentally unobtainable. However, in 2010 it was discovered that for sufficiently steep rotation profiles the AMRI switches to the same inductionless  $(Re, Ha)$  parameter values as the HMRI [11]. It is this inductionless version of the AMRI that will be explored in this Letter.

The question of which parameters,  $(Rm, S)$  or  $(Re, Ha)$ , are the relevant ones, and how that might vary depending on the steepness of the rotation profile, is also of potential astrophysical significance, since the Keplerian profile  $\Omega(r) \propto r^{-3/2}$  that is of greatest interest in accretion disks is considerably shallower than the limiting Rayleigh value  $\Omega(r) \propto r^{-2}$ . For the azimuthal field profile  $B_\phi \propto r^{-1}$  both the HMRI as well as the AMRI have switched from  $(Re, Ha)$  back to  $(Rm, S)$  for rotation profiles as shallow as Keplerian, as was first noted for the HMRI by Liu *et al.* [12] and generalized to higher  $m$  modes by Kirillov *et al.* [13]. However, if the field profiles are taken only slightly shallower than  $B_\phi \propto r^{-1}$ , both the HMRI and the AMRI have recently been shown [14] to scale with  $(Re, Ha)$  even for Keplerian rotation profiles. The astrophysical importance of these  $(Rm, S)$  versus  $(Re, Ha)$  scaling laws thus continues to be an open question.

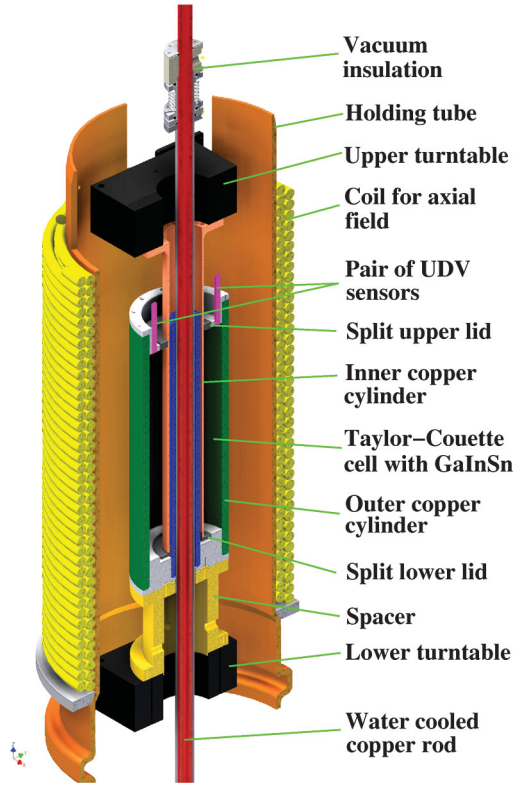


FIG. 1 (color). Sketch of the experimental setup.

In order to study this nonaxisymmetric AMRI, we utilize a slightly modified version of the PROMISE facility which has previously been used for investigations of the HMRI [15]. The main part of PROMISE is a cylindrical vessel (Fig. 1) made of two concentric copper cylinders enclosing a cylindrical volume of width  $d = r_{\text{out}} - r_{\text{in}} = 40$  mm, between the radii  $r_{\text{in}} = 40$  mm and  $r_{\text{out}} = 80$  mm, and a height of 400 mm. This cylindrical volume is filled with the liquid eutectic alloy  $\text{Ga}^{67}\text{In}^{20.5}\text{Sn}^{12.5}$  for which  $\text{Pm} = 1.4 \times 10^{-6}$ . Both the upper and lower end caps of the cylindrical volume are formed by two plastic rings, separated at  $r = 56$  mm, the inner and outer ring rotating with the inner and outer cylinders, respectively.

The magnetic field configuration is basically identical to that of the previous PROMISE experiments, apart from a significant enhancement of the power supply that now allows for currents in the central copper rod of up to 20 kA. This value is approximately double the expected critical value for the onset of AMRI [3,11]. The central rod can become quite hot, and was therefore thermally insulated by a vacuum tube to prevent any convection effects in the fluid. This vertical copper rod is connected to the power source by two horizontal rods at a height of 0.8 m below the bottom and above the top of the cylindrical volume. The slight deviation from a purely axisymmetric  $B_\phi(r)$  that arises from this asymmetric wiring will play an important role below. We further mention that the coil for the production of the axial field

$B_z$  was left in place, although it was not used for the particular experiments reported in this Letter. In any case, there is no electrical current applied to the liquid metal, in contrast to previous experiments on the pinch-type Taylor instability [16].

With  $B_z$  being set to zero, the AMRI is completely governed by only three nondimensional parameters, the Reynolds number  $\text{Re} := \Omega_{\text{in}} d r_{\text{in}} / \nu$ , the ratio of outer to inner angular frequencies  $\mu := \Omega_{\text{out}} / \Omega_{\text{in}}$ , and the Hartmann number characterizing the azimuthal magnetic field:  $\text{Ha} := B_\phi(r_{\text{in}}) (r_{\text{in}} d \sigma / \rho \nu)^{1/2}$ . For converting between dimensional and nondimensional quantities we can use the following relations:  $\text{Re} = 4710 \Omega_{\text{in}} / \text{s}^{-1}$  and  $\text{Ha} = 7.77 I_{\text{rod}} / \text{kA}$ .

The measuring instrumentation consists of two ultrasonic Doppler velocimetry (UDV) transducers (from Signal Processing SA) working at a frequency around 3.5 MHz, which are fixed into the outer plastic ring, 12 mm away from the outer copper wall, and flush mounted at the interface to the GaInSn. The signals from these sensors are transferred from the rotating frame of the outer cylinder to the laboratory frame by means of a slip ring contact which is situated below the vessel (not shown in Fig. 1). The UDV provides profiles of the axial velocity  $v_z$  along the beam lines parallel to the axis of rotation. The spatial resolution in the axial direction is around 1 mm; the time resolution is 2 sec.

From previous work [3,11] we anticipate that the AMRI starts at  $\text{Ha} \approx 80$  and manifests itself as a nonaxisymmetric ( $m = \pm 1$ ) spiral velocity structure that rotates around the vertical axis with an angular frequency close to that of the outer cylinder. This  $m = \pm 1$  mode can be identified by taking the difference of the signals of the two UDV transducers, although the observed frequency in the corotating frame of the sensors will be rather small. Among other numerical tools [3], we have used the OpenFOAM library, enhanced by a Poisson solver for the determination of the induced electric potential (see Ref. [17] for details), in order to simulate the AMRI for the true geometry of the facility and the real Pm of GaInSn. The velocity structure simulated in this way can then be transformed to the corotating frame in order to compare the resulting velocity pattern with the experimentally observed one.

This is done in Figs. 2 and 3, for  $\mu = 0.26$ ,  $\text{Re} = 1480$ , and  $\text{Ha} = 77$ , and  $\text{Ha} = 110$ , respectively. For the idealized case of a perfectly axisymmetric  $B_\phi(r)$ , Fig. 2(a) illustrates the simulated  $m = \pm 1$  projection of the axial velocity perturbation  $v_z(z, t)$  in dependence on time  $t$  and vertical position  $z$ , when virtually transformed to the corotating frame of the UDV sensors. The resulting “butterfly” pattern represents a spiral, rotating slightly faster than the outer cylinder, whose energy is concentrated approximately in the middle parts of the upper and lower halves of the cylinder. In Fig. 2(b) we show the simulation for the real geometry of the applied magnetic field, including its slight symmetry breaking due to the one-sided wiring (the

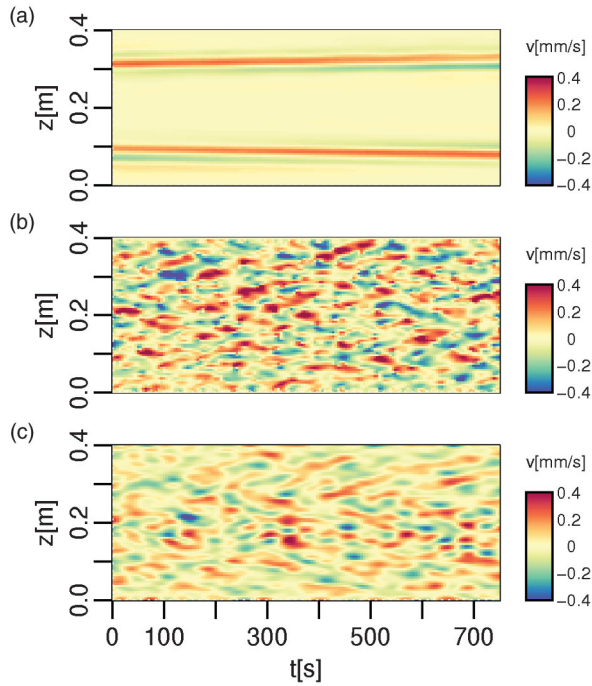


FIG. 2 (color). Velocity perturbation  $v_z(m=1, z, t)$  for  $\mu = 0.26$ ,  $\text{Re} = 1480$ , and  $\text{Ha} = 77$ . (a) 3D simulation for ideal axisymmetric field. (b) 3D simulation for realistic field. (c) Experimental results.

deviation is about 5 percent at the inner radius, and 10 percent at the outer radius). The effect is remarkable: the formerly clearly separated spiral structures now also fill the middle part of the cylinder and penetrate into the other halves (a comparable effect in which individual left- and right-spiral waves are replaced by interpenetrating spirals has been investigated in connection with the double Hopf bifurcation in a corotating spiral Poiseuille flow [18]). The corresponding velocity pattern observed in the experiment is shown in Fig. 2(c); the similarity to the realistic simulation in Fig. 2(b) is striking. Note that in both Figs. 2(b) and 2(c) we have filtered out those components of the  $m = \pm 1$  modes that are stationary in the laboratory frame, since they are a direct consequence of the external symmetry breaking, without any relation to the AMRI mode as such.

The same procedure is documented for  $\text{Ha} = 110$  in Fig. 3. Again, Fig. 3(a) shows the numerically computed pattern for the perfectly axisymmetric case. The “butterfly diagram” has now changed its direction, meaning that the spiral rotates slightly slower than the outer cylinder. The more realistic simulation in Fig. 3(b) shows the interpenetration of the spirals of the upper and lower halves of the cylinder, which is also qualitatively confirmed by the experimental data in Fig. 3(c).

By analyzing a total of 102 experimental runs similar to those documented in Figs. 2(c) and 3(c), we have extracted the dependence of various quantities on  $\text{Ha}$ . For  $\mu = 0.26$

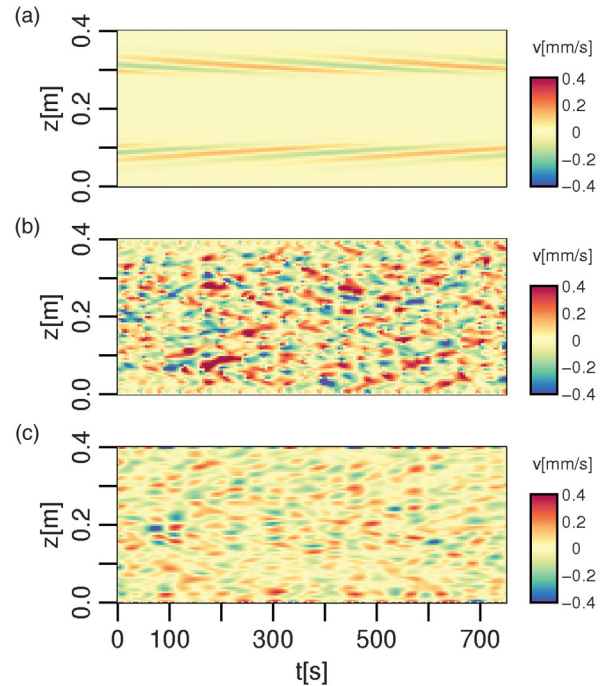


FIG. 3 (color). As in Fig. 2, but for  $\text{Ha} = 110$ .

and  $\text{Re} = 1480$ , Fig. 4(a) shows the theoretical growth rate of the AMRI as determined by a 1D-eigenvalue solver for the infinite length system [3]. In Fig. 4(b) we show then the mean square value of the UDV-measured velocity perturbation  $v_z(m=1, z, t)$  and compare them with the numerically determined ones for the idealized axisymmetric and the realistic applied magnetic fields. Whereas the growth rate in Fig. 4(a) and the numerical rms results under the axisymmetric field condition give a consistent picture with a sharp onset of AMRI at  $\text{Ha} \approx 80$  [3,11], the slight symmetry breaking of the field leads, first, to some smearing out of the rms for lower  $\text{Ha}$  and, second, to a significant increase of the rms velocity value, with a reasonable correspondence of numerical and experimental values. The remaining deviation of the rms value might have to do with the smoothing and filtering processes that are necessary due to the high noise level of the raw data from the UDV (which is indeed at the edge of applicability here), as well as with some compromises made in the numerical simulation, in particular with respect to the complicated electrical boundary conditions.

The dependence of the numerically and experimentally determined normalized drift frequency on  $\text{Ha}$  is shown in Fig. 4(c). AMRI represents an  $m = \pm 1$  spiral pattern that rotates approximately with the rotation rate of the outer cylinder [3]. There is still some deviation from perfect corotation, with a slightly enhanced frequency for lower  $\text{Ha}$  and a slightly reduced frequency for higher  $\text{Ha}$ , which can be identified both in the linear theory and in the experimental data. The corresponding wave numbers are presented in Fig. 4(d).

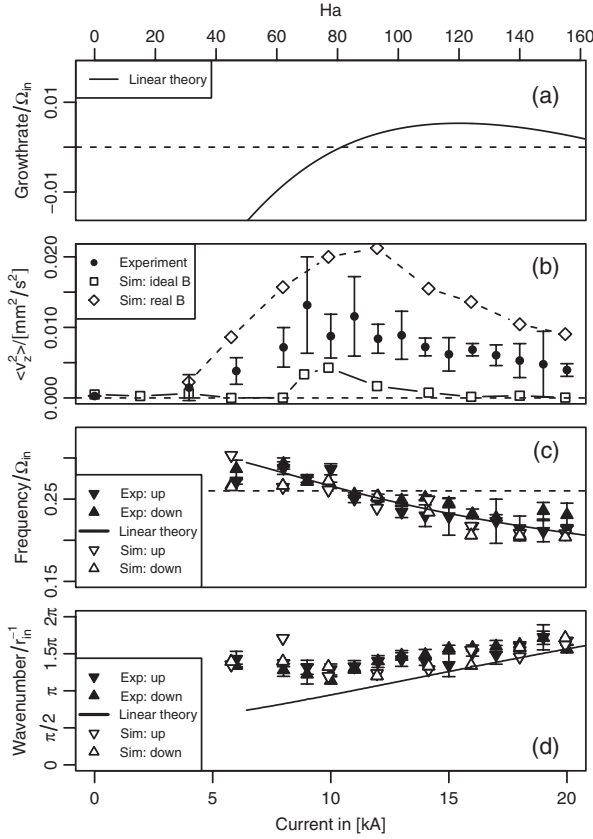


FIG. 4. Results for  $Re = 1480$ . (a) Growth rate from a 1D linear stability code, (b) mean square velocity perturbation from experiment and two different 3D simulations for idealized and real magnetic field geometry, (c) angular drift frequency, and (d) wave number from experiment, from the 1D linear stability code, and from the 3D simulation with real field geometry. The error bar of the velocity perturbation corresponds to an 85 percent confidence level. The “up” and “down” values in (c) and (d), which refer to the travel direction of the velocity perturbations as exemplified in Figs. 2 and 3, are determined by a center-of-gravity method applied to the 2D FFT of the data.

For a doubled rotation rate, i.e.,  $Re = 2960$ , Fig. 5 shows the same quantities as in Fig. 4, except with the numerical predictions restricted to those of the 1D eigenvalue solver, since 3D simulations already become extremely expensive in this case. Still, the qualitative behavior of the rms and the frequency agrees well with that at the lower rotation rates (Fig. 4).

In summary, we have shown that AMRI occurs in a hydrodynamically stable differential rotational flow of a liquid metal when it is exposed to a dominantly azimuthal magnetic field. The critical Hartmann number for the onset of AMRI is close to the numerically predicted value of approximately 80. The dependence of the rms, the drift frequency, and the axial wave number of the nonaxisymmetric velocity perturbations on  $Ha$  turned out to be in good agreement with numerical predictions, especially if the latter incorporate the surprisingly strong effect of the slight

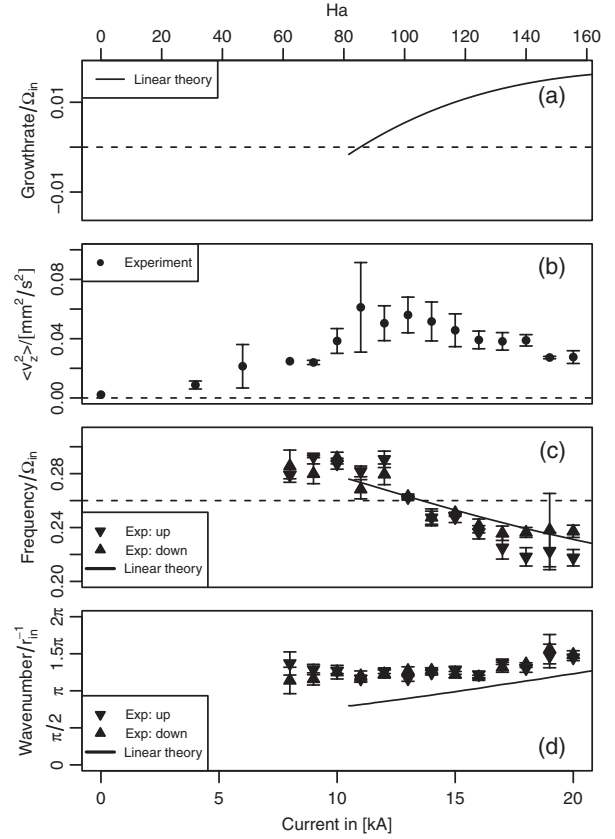


FIG. 5. As in Fig. 4 (except the 3D simulation data), but for  $Re = 2960$ .

symmetry breaking of the externally applied magnetic field. This underlines the importance of 3D codes, working at realistic  $Pm$ , for a detailed understanding of experimental results. Presently, experimental and numerical work is going on to scrutinize the dependence of the AMRI on the ratio  $\mu$  of outer to inner cylinder rotation rates. The main focus here is on whether the (modified) AMRI could possibly extend to rotation profiles as flat as the Keplerian one.

Significantly more experimental effort is needed to study the influence of an additionally applied  $B_z$ , which breaks the symmetry between the  $m = 1$  and  $m = -1$  modes [11]. When increasing  $B_z$  even further [at  $B_z \approx 0.05B_\phi(r_{in})$ , see Fig. 3 of Ref. [11]], we should also be able to observe the transition from the  $m = \pm 1$  AMRI mode back to the previous  $m = 0$  HMRI mode which can be identified in the sum of the signals of the two UDV transducers [15]. A more ambitious project, planned within the framework of the DRESYDYN project [19], will comprise a large liquid sodium experiment for the combined investigation of SMRI, HMRI, AMRI, and the current-driven Tayler instability [16].

This work was supported by the Helmholtz-Gemeinschaft Deutscher Forschungszentren (HGF) in the framework of the Helmholtz Alliance LIMTECH, as well

as by the Deutsche Forschungsgemeinschaft under SPP 1488 (PlanetMag). M. S. would like to thank Hans Georg Krauthäuser for many discussions on data analysis problems. Technical support by Steffen Borchardt, Heiko Kunath, and Bernd Nowak is gratefully acknowledged.

---

\*F.Stefani@hzdr.de

- [1] E. P. Velikhov, *Sov. Phys. JETP* **9**, 995 (1959).
- [2] S. A. Balbus and J. F. Hawley, *Astrophys. J.* **376**, 214 (1991).
- [3] G. Rüdiger, M. Gellert, M. Schultz, R. Hollerbach, and F. Stefani, *Mon. Not. R. Astron. Soc.* **438**, 271 (2014).
- [4] A. Brandenburg, A. Nordlund, R. F. Stein, and U. Torkelsson, *Astrophys. J.* **446**, 741 (1995); F. Rincon, G. I. Ogilvie, and M. R. E. Proctor, *Phys. Rev. Lett.* **98**, 254502 (2007); J. Hecart, F. Rincon, C. Cossu, G. Lesur, G. I. Ogilvie, and P.-Y. Longaretti, *Phys. Rev. E* **84**, 036321 (2011).
- [5] P. Eggenberger, J. Montalban, and A. Miglio, *Astron. Astrophys.* **544**, L4 (2012).
- [6] S. Fromang and J. Papaloizou, *Astron. Astrophys.* **476**, 1113 (2007); P. J. Käpilä and M. J. Korpi, *Mon. Not. R. Astron. Soc.* **413**, 901 (2011).
- [7] R. Hollerbach and G. Rüdiger, *Phys. Rev. Lett.* **95**, 124501 (2005).
- [8] D. R. Sisan, N. Mujica, W. A. Tillotson, Y.-M. Huang, W. Dorland, A. B. Hassam, T. M. Antonsen, and D. P. Lathrop, *Phys. Rev. Lett.* **93**, 114502 (2004); M. D. Nornberg, H. Ji, E. Schartman, A. Roach, and J. Goodman, *Phys. Rev. Lett.* **104**, 074501 (2010).
- [9] G. I. Ogilvie and J. E. Pringle, *Mon. Not. R. Astron. Soc.* **279**, 152 (1996).
- [10] G. Rüdiger, R. Hollerbach, M. Schultz, and D. Elstner, *Mon. Not. R. Astron. Soc.* **377**, 1481 (2007).
- [11] R. Hollerbach, V. Teeluck, and G. Rüdiger, *Phys. Rev. Lett.* **104**, 044502 (2010).
- [12] W. Liu, J. Goodman, I. Herron, and H. Ji, *Phys. Rev. E* **74**, 056302 (2006).
- [13] O. N. Kirillov, F. Stefani, and Y. Fukumoto, *Astrophys. J.* **756**, 83 (2012).
- [14] O. N. Kirillov and F. Stefani, *Phys. Rev. Lett.* **111**, 061103 (2013).
- [15] F. Stefani, T. Gundrum, G. Gerbeth, G. Rüdiger, M. Schultz, J. Szklarski, and R. Hollerbach., *Phys. Rev. Lett.* **97**, 184502 (2006); F. Stefani, T. Gundrum, G. Gerbeth, G. Rüdiger, J. Szklarski, and R. Hollerbach, *New J. Phys.* **9**, 295 (2007); F. Stefani, G. Gerbeth, T. Gundrum, R. Hollerbach, J. Priede, G. Rüdiger, and J. Szklarski, *Phys. Rev. E* **80**, 066303 (2009).
- [16] M. Seilmayer, F. Stefani, T. Gundrum, T. Weier, G. Gerbeth, M. Gellert, and G. Rüdiger, *Phys. Rev. Lett.* **108**, 244501 (2012).
- [17] N. Weber, V. Galindo, F. Stefani, T. Weier, and T. Wondrak, *New J. Phys.* **15**, 043034 (2013).
- [18] M. Avila, A. Meseguer, and F. Marques, *Phys. Fluids* **18**, 064101 (2006).
- [19] F. Stefani, S. Eckert, G. Gerbeth, A. Giesecke, Th. Gundrum, C. Steglich, T. Weier, and E. Wustmann, *Magnetohydrodynamics* **48**, 103 (2012).